Proceedings of the ASME 2021
International Design Engineering Technical Conferences and
Computers and Information in Engineering Conference
IDETC-CIE2021
August 17-19, 2021, Virtual, Online

DETC2021-67670

A STUDY OF THE MULTI-STABILITY IN A NON-RIGID STACKED MIURA-ORIGAMI CELLULAR MECHANISM

Jiayue Tao[*], **and Suyi Li**
Department of Mechanical Engineering, Clemson University
Clemson, South Carolina 29634

ABSTRACT

Multi-stable structures have gathered extensive interest because they can provide a broad spectrum of adaptive functions for many engineering systems. Especially, origami sheets with a translational periodicity can be stacked and assembled to form a multi-stable cellular solid, which has emerged as a promising platform to design functional structures. This paper investigates the multi-stability characteristics of a non-rigid stacked Miura-origami mechanism consisting of Miura-ori sheets and accordion-shaped connecting sheets, focusing on the elemental unit cell. A nonlinear mechanical model based on the bar-hinge approach is established to quantitatively study the unit cell's multi-stability with intentionally relaxed rigid-folding conditions. Results show that only two stable states are achievable in the unit cell with enforced rigid-folding kinematics. However, if one relaxes the rigid-folding conditions and allows the facet to deform (i.e.. non-rigid folding), four stable states are reachable in the unit cell if the crease torsional stiffness of the connecting sheets becomes sufficiently larger than that of the Miura-ori sheets, or the stress-free folding angle deviates away from 0°. A close examination of the potential energy composition of the non-rigid unit cell provides a detailed principle underpinning the multi-stability. By showing the benefits of exploiting facet compliance, this study can become the building blocks for origami-based structures and material systems with a wider variety of novel functionalities.

Keywords: Multi-stability; Non-rigid origami

Nomenclature

α, β	Relative facet rigidity ratio of the Miura-ori sheets and the connecting sheets
η	Sign indicator.
$\mathbf{K}_S$, $\mathbf{K}_F$, $\mathbf{K}_B$	Tangent stiffness matrix corresponding to the bar stretching, crease folding and facet bending.
$\mathbf{m}$, $\mathbf{n}$	Surface normal vectors.
$\mathbf{u}$	Nodal displacement vector.
Π	Total potential energy of the unit cell.
$\mathbf{B}_1$, $\mathbf{B}_2$	Compatibility vector and matrix.
$\mathbf{e}_1$	Unit vector $[1,0,0]$.
$\mathbf{I}_{3\times3}$	3-by-3 identity matrix.
θ_k	Dihedral folding angles between the Miura-ori facets and the $x-y$ reference plane, k = I, II.
θ_k^0	Initial folding angle.
φ	Dihedral angle between two adjacent triangles.
a_k, b_k , γ_k	Geometrical design parameters of Miura-ori sheets, k = I, II.
F_c	Required compression force to trigger the switching from state (2) to (1).
F_e	Required extension force to trigger the switching from state (1) to (2).
k_S	Axial rigidity of the bar element.
$k_{f\mathrm{CM}}$	Torsional stiffness per unit length along the creases between the connecting sheets and the Miura-ori sheets.
$k_{f\mathrm{C}}$	Torsional stiffness per unit length along the creases in the connecting sheets.
$k_{f\mathrm{M}}$	Torsional stiffness per unit length of the creases in Miura-ori sheets I and II.

---

[*] Address all correspondence to this author: jiayuet@clemson.edu

L	Total length of the unit cell along the z-axis.
l_c	Length of the connecting sheets along the z-axis.
M_f, M_b	Rotational resistance moment due to crease folding and facet bending.
U_S, U_F, U_B	Internal strain energy from bar stretching, crease folding, and facet bending
W_{ext}	Work done by external forces.
$k_{b\mathrm{C}}$	Facet bending stiffness per unit length of the semi-diagonal line in connecting sheets.
$k_{b\mathrm{M}}$	Facet bending stiffness per unit length of the semi-diagonal line in Miura-ori sheets I and II.

1 INTRODUCTION

An engineered structure or material system is considered multi-stable when it possesses more than one stable equilibrium (or stable states), and it can settle in any one of its states without external aids. Recently, multi-stable structures and material systems have received extensive interests because they can provide a wide variety of adaptive functions, such as wave propagation control [1, 2], shape morphing [3], stiffness adaptation [4], impact energy absorption [5], and robust sensing [6]. Many well-studied multi-stable mechanisms have seen their applications in robotics [7], morphing aircraft [8], and energy harvesting devices [9].

While the method of achieving multi-stability is quite diverse, origami — an ancient craftsman art of folding paper — has emerged as a promising platform [10, 11]. Origami folding has been transformed into a design framework to construct architected structures and material systems with many interesting mechanical properties, such as tunable Poisson's ratio [12], programmable nonlinear stiffness [13], and multi-stability [11].

Two different types of origami can exhibit multi-stability: one is rigid-foldable, and the other is not. By design, the folding kinematics of rigid-foldable origami only require rotation along its crease lines. Therefore, this type of origami can be treated as three-dimensional linkage mechanism consisting of rigid facets connected via hinge-like creases. As a result, multi-stability arises via the combination of nonlinear folding kinematics and purposefully assigned torsional stiffness on the creases [10]. For example, Fang et al. constructed a cellular structure by assembling unit cells consisting of two different Miura-ori sheets. These two Miura-ori sheets maintain their rigid-foldability based on the geometric compatibility, and bi-stability is achievable when their crease torsional stiffness differs significantly [14]. Other rigid-foldable and multi-stable origami include leaf-out [15] and water-bomb pattern [16].

On the other hand, non-rigid foldable origami can also be multi-stable by leveraging their facet deformations between different folding configurations. A classic example is a Kresling origami [17]. Its triangular facets are flat at the "deployed" and "compressed" configurations, but the facets must bend as the Kresling folds between these two states. Other non-rigid foldable and multi-stable origami include the square twist pattern [18] and star pattern [19].

However, the distinctions between rigid-foldable and non-rigid foldable origami are not strict. Rigid-foldable origami can exhibit non-rigid folding behavior in practical applications due to the inevitable compliance in their facets and fabrication imperfections [20]. Such compliance in the facet can indeed allow the origami to access the otherwise unavailable folding configurations. As a result, new multi-stability characteristics can arise. This study demonstrates this principle by intentionally relaxing the rigid-folding constraints of a stacked Miura-ori cellular structure examined by the authors' previous paper [21]. Numerical simulation based on the nonlinear bar-hinge model [20] shows that a unit cell of a stacked origami can switch among four distant stable states with appropriate compliance in the facets.

The rest of this paper is organized as follows. Section 2 briefly reviews the stacked origami's unit cell geometry and discusses its rigid folding kinematics. Section 3 summarizes the formulation of the nonlinear mechanics model for the unit cell considering the compliance of facets. We apply the nonlinear bar-hinge approach developed by Liu and Paulino to examine the origami unit cell's multi-stability characteristics under large deformation [22]. Section 4 details the origin of such multi-stability by comparing the unit cell with or without the rigid folding assumption. Finally, section 5 ends this paper with a summary and discussion. This paper's results can foster new approaches to enrich the mechanical properties of origami-based structures and materials by strategically manipulating facet compliance.

2 DESIGN AND RIGID-FOLDING KINEMATICS

This study focuses on a stacked origami cellular structure consisting of multiple alternatively arranged unit cells as shown in Figure 1(a). The most fundamental component of this cellular origami is the unit cell consisting of two types of Miura-ori sheets and the connecting sheets, as shown in Figure 1(b). The unit cell here is essentially a variation of the stacked-origami unit cell proposed by other studies [14], with a reversed arrangement of Miura-ori sheet I and II and the additional accordion-shaped connecting sheets.

The geometries of the unit cell can be defined by two types of parameters [12]. One is the geometric design parameters of the constituent Miura-ori sheets, including the crease lengths (a_k and b_k) and sector angle (γ_k), where the subscript k (= I or II) denotes the Miura-ori sheet I and II, respectively, as shown in Figure 1(c). l_c is the length of the connecting sheets along the z-axis. The other type of parameters is the kinematic folding angles θ_k, defined as the dihedral angles between the facets of Miura-ori sheet I or II and the $x-y$ reference plane, respectively. Here, θ_k is denoted as positive if the corresponding Miura-ori sheet is "above" the $x-y$ plane and negative otherwise. The resting, stress-free

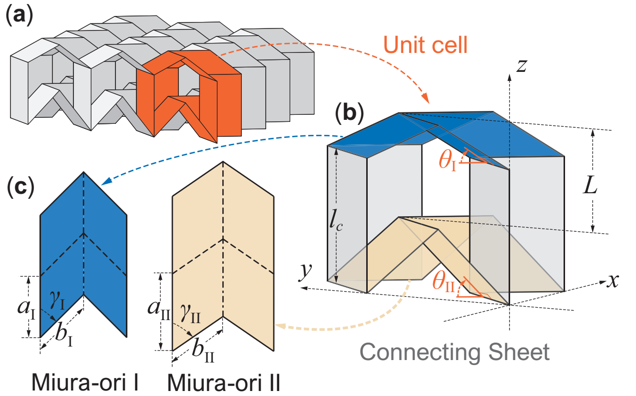

FIGURE 1: Design of the multi-stable stacked origami cellular structure. (a) An overview showing the alternating stacking of unit cells. (b) A close-up view of the elementary unit cell, which consists of two different Miura-ori sheets and the accordion-shaped connecting sheets. The dihedral folding angles θ_I or θ_{II} are defined between the facets of Miura-ori sheet I or II and the $x-y$ reference plane, respectively. (c) The geometric design parameters of Miura-ori sheets I, II.

stable state of the unit cell is defined at $\theta_I = \theta_I^0$ and $\theta_{II} = \theta_{II}^0$, where no creases or facets are subject to deformation. To ensure geometric compatibility according to rigid-folding conditions, the design parameters should satisfy the constraints that $b_I = b_{II}$, $a_I \cos\gamma_I = a_{II}\cos\gamma_{II}$ (Here, we assume Miura-ori sheet II is bigger in that $a_{II} > a_I$) [12, 23].

If the stacked Miura-ori cell follows the rigid folding kinematics, there is no stretching, bending, or twisting deformation in the facets of Miura-ori and connecting sheets. The two folding angles are not independent but rather satisfy the kinematic constraint in that $\cos\theta_I \tan\gamma_I = \cos\theta_{II}\tan\gamma_{II}$. Therefore, the rigid-folding motion has only one degree-of-freedom. The total length L of the unit cell along the z-axis can be calculated as the distance between the center points of the two Miura-ori sheets:

$$L = a_I \sin\theta_I \sin\gamma_I - a_{II}\sin\theta_{II}\sin\gamma_{II} + l_c. \tag{1}$$

This rigid-folding stacked origami unit cell has two distinct and disconnected kinematic "paths" according to these rigid-folding conditions, as shown in Figure 2 (the corresponding origami design parameters are shown in Table 1). On path A, the larger Miura-ori sheet II is "nested-in" so that $\theta_{II} > 0\circ$, while on path B, Miura-ori sheet II is "bulged-out" so that $\theta_{II} < 0\circ$. If the rigid-folding conditions are strictly reinforced, the stacked origami unit cell's deformation cannot deviate from these two paths. As a result, it cannot deform from one kinematic path to the other.

On the other hand, if we relax the rigid-folding constraints and allow compliance in both the Miura-ori sheets and the connecting sheets, the origami facets behave like shell elements with complex deformation. Therefore, the non-rigid stacked origami cells allow richer deformation characteristics by deforming away from the two kinematic paths. In this study, we examine the underlying principles of multi-stability in such non-rigid origami mechanisms.

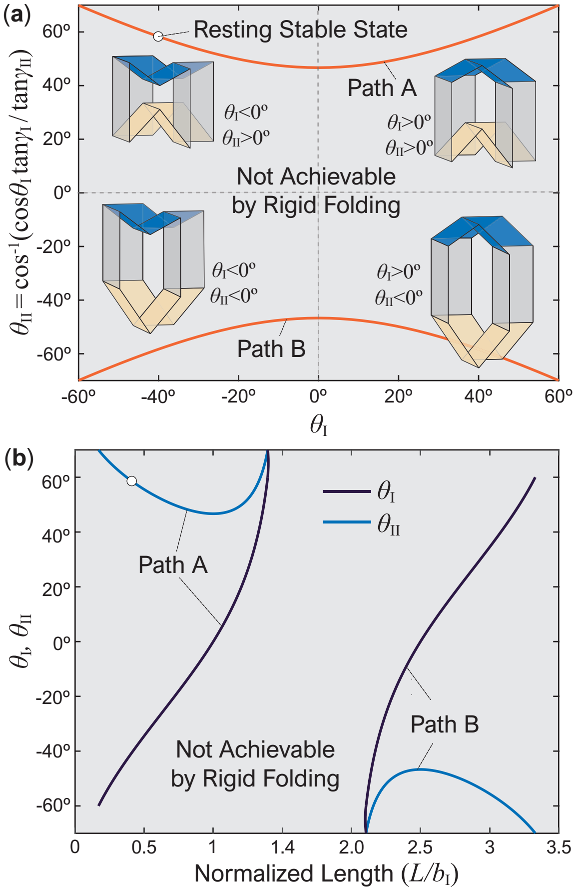

FIGURE 2: The kinematic paths of the unit cell under rigid-folding conditions. (a) The kinematic path is based on the relationship between the folding angles of two Miura-ori sheets. Here, the subplots illustrate folding configurations on different sections of these paths. (b) The kinematic paths based on the total unit cell length. The gray shaded regions are physically unavailable because of the kinematic constraint due to the rigid-folding assumption.

3 NON-RIGID FOLDING MECHANICS MODELING

This section briefly summarizes the formulation of a nonlinear mechanics model for the stacked Miura-ori cell without rigid-folding constraints. This model is based on the nonlinear bar-hinge approach proposed by Liu and Paulino [22], and interested readers can refer to the relevant literature for further details [20, 24].

TABLE 1: Design parameters of the stacked origami unit cell

Geometry	Value	Material	Value
a_{I}	20 mm	$k_{f\mathrm{M}}$	0.05 N/rad
a_{II}	25 mm	$k_{f\mathrm{CM}}$	0.05 N/rad
$b_{\mathrm{I}}(=b_{\mathrm{II}})$	20 mm	$k_{f\mathrm{C}}$	12 N/rad
l_c	35 mm	k_s	10^4 N
γ_{I}	45°	α	$100\sim10^5$
θ_{I}^0	−40°	β	$100\sim10^5$

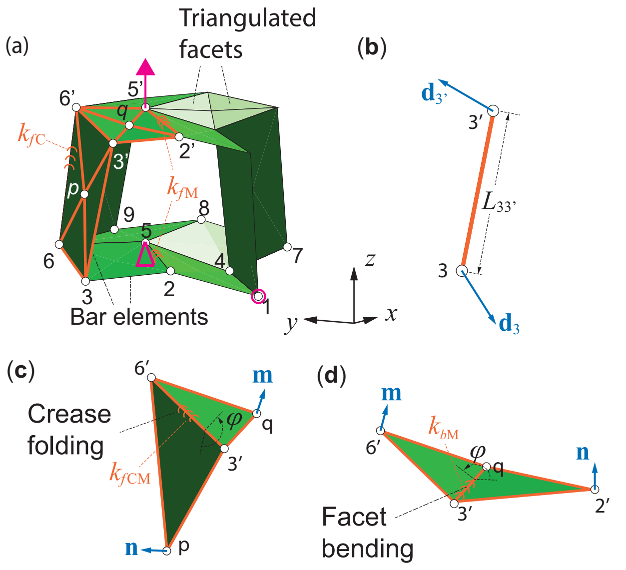

FIGURE 3: Formulation of the mechanics model for the unit cell. (a) The N5B8 mesh scheme in the unit cell based on the bar-hinge approach. Here, $k_{f\mathrm{M}}$, $k_{f\mathrm{C}}$ represent the linear torsional stiffness per unit length of the crease folding in Miura-ori and connecting sheet, respectively. The solid lines represent the stretchable bar elements, and hollow circles represent pin-joints. (b) The formulation of a bar element. (c) The formulation of the folding hinge along the crease $3'-6'$. $k_{f\mathrm{CM}}$ represents the linear torsional stiffness per unit length of the creases between the connecting sheets and the Miura-ori sheets. (d) The formulation of the bending hinge between two triangular facets, where $k_{b\mathrm{M}}$ represents the linear torsional stiffness per unit length of the facet bending along the semi-diagonal line $3'-q$. In this model, node 5 (highlighted by the magenta triangle) is fully constrained with no displacement in x, y, or z-directions. Node 1 (highlighted by the magenta circle) is allowed to displace only in the y and z-direction. We apply controlled z-directional displacement at node $5'$.

3.1 Model Formulation Fundamentals

The bar-hinge approach discretizes the continuous origami structure into a pin-jointed truss-frame mechanism [12, 25, 26]. It uses stretchable bar elements to represent the origami crease and to diagonalize the facets. To estimate crease folding and facet bending, this model adds rotational stiffness between the triangles defined by these trusses. The reduced-order model can analyze different origamis' primary deformations without incurring expensive computational cost like in the finite element simulations. This study uses the open-source MERLIN2 software to simulate unit cell's multi-stability under the displacement control (N5B8 scheme) (Figure 3(a)) [20].

We assume the bar-hinge system's potential energy is conservative, so it is only a function of the current configuration. Therefore, the principle of stationary potential energy, which accounts for both constitutive material properties and nonlinear folding kinematics, can be used to derive the equilibrium equations and tangent stiffness matrix. The total potential energy Π of the unit cell has contributions from the internal strain energy, including bar stretching energy (U_S), crease folding energy (U_F), facet bending/twisting energy (U_B), as well as the external mechanical work done by applied forces (W_{ext}) so that

$$\Pi = U_S + U_F + U_B - W_{ext}. \tag{2}$$

A critical step in formulating the unit cell's mechanics model is to obtain the tangent stiffness matrix (aka. a second-order approximation of the potential energy Π) as [22, 27]

$$\mathbf{K} = \mathbf{K}_S + \mathbf{K}_F + \mathbf{K}_B, \tag{3}$$

where the three terms on the right-hand side are stiffness from bar stretching, crease folding, and facet bending, respectively. For example, $\mathbf{K}_S$ represents the in-plane stretching and shearing stiffness of the bar elements. Taking the bar element connecting pin-joints 3 and $3'$ as an example (Figure 3(b)), one can define the bar stretching energy as

$$U_S^{33'} = \int_0^{L^{33'}} WAdX, \tag{4}$$

where A is the bar element's cross-section area, $L^{33'}$ is the current bar length, and W is the energy density, which is a function of the one dimensional Green-Lagrange strain $E_{xx} = \mathbf{B}_1\mathbf{u}^{33'} + 0.5\mathbf{u}^{(33')T}\mathbf{B}_2\mathbf{u}^{33'}$. Here, the displacement vector of the bar element $\mathbf{u}^{33'} = \left[\mathbf{d}_3^T \ \mathbf{d}_{3'}^T\right]^T$, $\mathbf{B}_1 = [-\mathbf{e}_1 \ \mathbf{e}_1]/L^{33'}$, $\mathbf{B}_2 = [\mathbf{I}_{3\times3} \ -\mathbf{I}_{3\times3}; -\mathbf{I}_{3\times3} \ \mathbf{I}_{3\times3}]/(L^{33'})^2$. $\mathbf{e}_1 = [1,0,0]$, and $\mathbf{I}_{3\times3}$ is the identity matrix of size 3 by 3. The tangent stiffness matrix components corresponding to this bar element is

$$
\begin{aligned}
\mathbf{K}_S^{33'} &= \frac{\partial^2 U_S^{33'}}{\partial \mathbf{u}^2} \\
&= k_s^{33'} L^{33'} \left(\mathbf{B}_1^T + \mathbf{B}_2 \mathbf{u}^{33'}\right)\left(\mathbf{B}_1^T + \mathbf{B}_2 \mathbf{u}^{33'}\right)^T + f^{33'} L^{33'} \mathbf{B}_2,
\end{aligned}
\tag{5}
$$

where $k_S^{33'}$ is the axial rigidity of the bar element, and $f^{33'}$ is the resultant longitudinal force. It is worth noting that this stiffness matrix involves both the linear term and nonlinear terms related to geometry and initial displacement [22]. One can then apply similar formulations to all bar elements and assemble the global bar stiffness matrix.

The rotational hinges with prescribed torsional spring stiffness coefficients are applied to the bar elements corresponding to the folding creases and bending facets to approximate their deformation. As shown in Figure 3(c-d), these torsional spring elements involve four vertices (nodes), five bars elements, and one dihedral angle between the two triangles defined by these bar elements.

Taking the rotational spring element corresponding to crease $3' - 6'$ as an example (Figure 3(c)). The crease folding energy is a function of the dihedral angle φ

$$U_F^{3'6'} = \psi_F^{3'6'}(\varphi), \tag{6}$$

where $\psi_F^{3'6'}$ is the energy function. The dihedral angle between the two adjacent triangles ($3' - 6' - p$ and $3' - 6' - q$) can be calculated as $\varphi = \eta \cos^{-1}\left(\frac{\mathbf{m}\cdot\mathbf{n}}{\|\mathbf{m}\|\|\mathbf{n}\|}\right)$, where the surface normal vectors $\mathbf{m} = \mathbf{r}_{3'q} \times \mathbf{r}_{q6'}$, $\mathbf{n} = \mathbf{r}_{3'p} \times \mathbf{r}_{p6'}$. The repeated indices do not imply summation in this paper. η is a sign indicator in that

$$\eta = \begin{cases} sgn(\mathbf{m}\cdot\mathbf{r}_{3'6'}) & \mathbf{m}\cdot\mathbf{r}_{3'6'} \neq 0 \\ 1 & \mathbf{m}\cdot\mathbf{r}_{3'6'} = 0 \end{cases}. \tag{7}$$

Because of the nonlinear geometric correlations among the dihedral angle (φ) and the nodal displacement vector ($\mathbf{u}$), the effective tangent stiffness is highly nonlinear even though its constituent creases are assumed to be linearly elastic in torsion [14]. The tangent stiffness matrix component corresponding to the crease folding is

$$\mathbf{K}_F^{3'6'} = \frac{\partial^2 U_F^{3'6'}}{\partial \mathbf{u}^2} = k_f L^{3'6'} \frac{d\varphi}{d\mathbf{u}} \otimes \frac{d\varphi}{d\mathbf{u}} + M_f \frac{d^2\varphi}{d\mathbf{u}^2}, \tag{8}$$

where $\otimes$ denotes the tensor product, $L^{3'6'}$ is the length of the crease $3' - 6'$, k_f is the torsional spring stiffness per unit length of the folding hinge, M_f is the rotational resistance moment, and $\mathbf{u}$ is the nodal displacement vector of the related pin-joints at the current configuration.

The same formulation applies to the torsional spring elements corresponding to facet bending hinges because they have the same kinematic structure as a folded crease. For example, in Figure 3(d), a torsional spring coefficient is assigned along the semi-diagonal of the quadrilateral facet (i.e., the bending line $3' - p$). The corresponding facet bending energy and tangent stiffness matrix are

$$U_B^{3'p} = \psi_B^{3'p}(\varphi) \tag{9}$$

$$\mathbf{K}_B^{3'p} = k_b L^{3'p} \frac{d\varphi}{d\mathbf{u}} \otimes \frac{d\varphi}{d\mathbf{u}} + M_b \frac{d^2\varphi}{d\mathbf{u}^2} \tag{10}$$

3.2 Material Property Selection

By the bar-hinge model, the origami unit cell's mechanics are directly related to the magnitude of bar stretching rigidity (k_s in Eq. 5), crease folding torsional stiffness (k_f in Eq. 8), and facet bending stiffness (k_b in Eq. 10). For clarity, we further divide the crease folding stiffness into different groups. $k_{f\mathrm{M}}$ is the torsional stiffness per unit length of the creases in Miura-ori sheets I and II. $k_{f\mathrm{CM}}$ is that of the creases between the connecting sheets and the Miura-ori sheets. $k_{f\mathrm{C}}$ is the torsional stiffness along the creases in the connecting sheets. The facet bending stiffness k_b can also be divided into two groups: $k_{b\mathrm{M}}$ for the Miura-ori facets and $k_{b\mathrm{C}}$ for the connecting sheet facets. Moreover, we assume all these stiffness coefficients are constant so that the non-linearity originates from the finite-amplitude deformation during folding. Unless stated otherwise, Table 1 summarizes the geometric and material parameters based on previous experiments [17].

In this study, the ratio between the facet bending stiffness and crease folding stiffness (aka., k_b/k_f) is crucial because it determines whether the origami follows the rigid-folding conditions [22]. A relatively large k_b/k_f ratio (e.g., 10^5) indicates that facets are relatively rigid with minimal deformation so that the rigid-folding kinematics dominate. In contrast, a small k_b/k_f ratio (e.g., 10) indicates a non-rigid foldable origami where the facet deformations are not negligible. Therefore, we define two ratios to describe the relative facet rigidity of the Miura-ori sheets and connecting sheets in that

$$\alpha = \frac{k_{b\mathrm{M}}}{k_{f\mathrm{M}}} \tag{11}$$

$$\beta = \frac{k_{b\mathrm{C}}}{k_{f\mathrm{C}}} \tag{12}$$

4 MULTI-STABILITY STUDY

This section discusses the stack-origami unit cell's multistability with different α and β ratios. The unit cell shown in

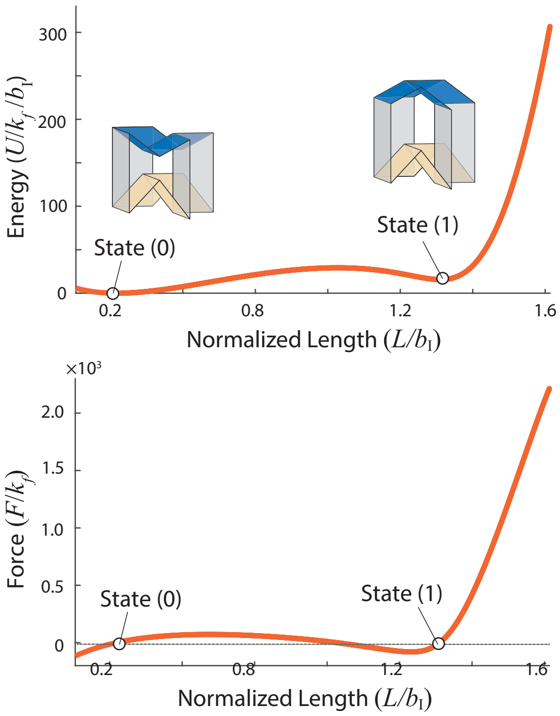

FIGURE 4: Bi-Stability in the rigid-foldable unit cell. (a) Elastic potential energy landscapes of the unit cell with only two stable states (0) and (1) exist. Here, the subplots roughly represent the corresponding folding configurations. (b) the force–displacement curves of the unit cell. Here, $\alpha = 10^5, \beta = 10^5$, and $k_{f\mathrm{C}}/k_{f\mathrm{M}} = 240$.

Figure 2 shows the initial stable state (0) with the initial folding angle $\theta_{\mathrm{I}}^0 = -40^\circ, \theta_{\mathrm{II}}^0 = 58^\circ$, where all creases and facets are stress-free without any deformations. Notice that the crease folding stiffness in the connecting sheet $k_{f\mathrm{C}}$ is significantly higher than other creases to ensure multi-stability, as shown in Table 1.

4.1 Bi-Stability With Rigid-Folding Condition

We first consider the case of rigid-foldable origami by setting α and β to 10^5 in the bar-hinge model. In this case, the internal strain energy in Eq. 2 only includes the crease folding energy in that $U = U_F$. As a result, if we stretch the unit cell along the z-axis under displacement control, it will switch from the initial stable state (0) to a new state (1) on the same kinematic path (Figure 4(a)). Such bi-stability is very similar to the authors' previous studies [21]. However, as we continue to stretch the unit cell, its reaction force will increase significantly due to the rigid facets (here, the reaction force is the first variation of strain energy with respect to the unit cell length, i.e., $F = \partial U/\partial L$). As a result, no other stable states are achievable.

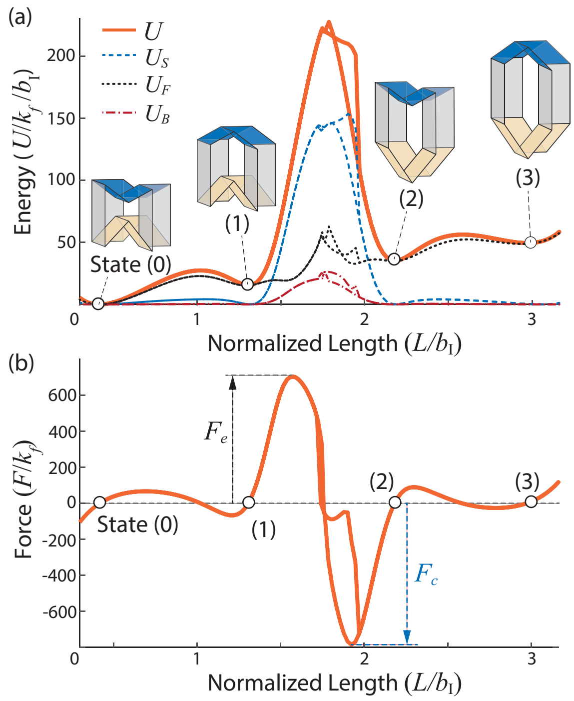

FIGURE 5: Multi-stability in the non-rigid unit cell. (a) the elastic potential energy landscapes, and (b) the corresponding reaction forces in this case of α = 100, β = 100, and $k_{f\mathrm{C}}/k_{f\mathrm{M}}$ = 240. Here, the subplots also roughly represent the corresponding folding configurations. Contributions from three deformation modes are highlighted, including the bar stretching energy U_S, crease folding energy U_F, and the facet bending energy U_B.

4.2 Multi-Stability Without Rigid-Folding Condition

As shown in the previous subsection, only two stable states exist in the unit cell under the rigid-folding condition, and the cell stays on kinematic path A, which is consistent with Figure 2. However, if we relax this rigid-folding assumption and allow compliance in the origami facets, more stable stables become reachable. Figure 5(a) illustrates the landscape of elastic potential energy U with respect to the unit cell length L, when $\alpha = 100$, $\beta = 100$, and $k_{f\mathrm{C}}/k_{f\mathrm{M}} = 240$. One can see that such compliance in origami facets allows the unit cell to deform from the kinematic path A to path B and access two new stable states (2) and (3).

It is worth noting that values of α and β in this proof-of-concept study (10^5 for the rigid origami and 100 for non-rigid origami) do not correspond to any particular material selections. Instead, they highlight the differences between the rigid and non-rigid origami so that we can illustrate the existence of additional multi-stability if we intentionally relax the rigid-folding conditions.

It is also worth noting that, as the unit cell extends from state (1) and (2), the Miura-ori sheet I inverts. This is because the Miura-ori sheet II is larger than sheet I in this study. As the unit cell extends from the state (1), the Miura sheet I is stretched almost flat. As a result, it tends to invert back to its initial stress-free configuration, and the unit cell switches to state (2) rather than directly to the state (3).

To provide further insights underpinning this new multi-stability, we plot the different strain energy components in Figure 5(a). As the unit cell switches between state (0) and (1), or between state (2) and (3), the crease folding energy U_f constitutes the majority of total strain energy. The unit cell roughly follows the rigid-folding kinematics between these two pairs of stable states because each pair is on the corresponding kinematic path. However, when the unit cell switches between state (1) and (2), the bar stretching energy and facet bending energy will play the dominant role, indicating that the unit cell has to violate the rigid-folding kinematics to deform between these two states. Since the facet stretching and bending give more resistance than crease folding, the magnitude of the energy barrier is the highest between stable states (1) and (2). A similar trend is evident in the corresponding reaction force plot in Figure 5(b). Here, we denote F_e as the required extension force to trigger the switching from states (1) to (2), and F_c as the required compression force to achieve the opposite switch. These two critical forces have the highest magnitudes.

Moreover, the energy and reaction force curves in Figure 5 show notable differences between the stretching and compression between the state (1) and state (2). This phenomenon is probably due to an "asymmetry" during the switch between these two states. That is, the origami unit cell induces larger bar stretching energy as it extends from the state (1) to state (2) than the opposite compression (Figure 5). More detailed origin and application of such asymmetry will be an interested topic for the future study.

Figure 6 shows the unit cell's potential energy landscapes with different design parameters. Generally speaking, multiple potential energy wells, which are the defining characteristics of a multi-stable system, start to show up as the connecting sheets' crease folding stiffness ($k_{f\mathrm{C}}$) is sufficiently larger than that of the Miura-ori sheets ($k_{f\mathrm{M}}$). Interestingly, if the connecting sheets' crease folding stiffness is only moderately higher than the Miura-ori sheets (e.g., $k_{f\mathrm{C}}/k_{f\mathrm{M}} = 40$ in Figure 6(a), the unit cell is only bi-stable at state (0) and state (2). This means that there is only one stable state on each kinematic path, and the energy barrier from the non-rigid folding separates these two states. As the $k_{f\mathrm{C}}/k_{f\mathrm{M}}$ ratio increases, the stable state (1) emerges from the kinematic path A so that the switching sequence $0 \leftrightarrow 1 \leftrightarrow 2$ is possible under cyclic loads. Finally, the stable state (3) appears as the $k_{f\mathrm{C}}/k_{f\mathrm{M}}$ increases further.

The effects of stress-free folding angle (θ_{I}^{0}) is shown in Figure 6(b). Here, we observe that as θ_{I}^{0} deviates further away from 0°, the required $k_{f\mathrm{C}}/k_{f\mathrm{M}}$ for achieving the same multi-stability is reduced.

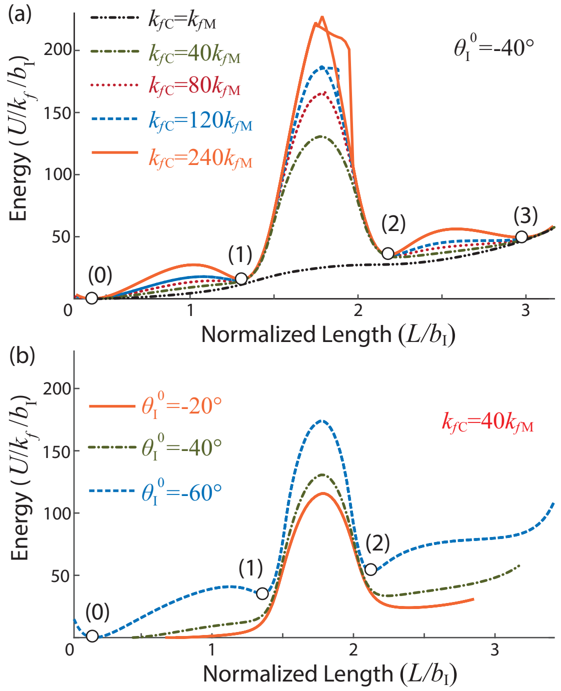

FIGURE 6: The potential energy landscapes of the unit cell based on different $k_{f\mathrm{C}}/k_{f\mathrm{M}}$ (a) and the stress-free resting folding angle θ_{I}^{o} (b). Here, $\alpha = 100, \beta = 100$.

5 SUMMARY AND CONCLUSIONS

This study examines the new multi-stability properties that emerge from intentionally relaxing the rigid-folding conditions in a stacked origami cellular structure. The unit cells in such a structure combine two different Miura-ori sheets and accordion-shaped connecting sheets. We conduct a quantitative analysis of the unit cell's multi-stability behavior based on the nonlinear bar-hinge approach. Here, we introduce two non-dimensional parameters α, β to describe the facets' relative rigidity in Miura-ori sheets and the connecting sheets, respectively, and simulate the multi-stable behavior based on two sets of parameters: high α, β for rigid-foldable origami and low α, β for non-rigid origami. The simulation results show that only two stable states exist in the unit cell if it satisfies the ideal rigid origami assumption. However, for a non-rigid origami mechanism, more stable states are reachable. The multi-stability starts to show up as the crease torsional stiffness of connecting sheets (i.e., $k_{f\mathrm{C}}$) becomes sufficiently larger than that of the Miura-ori sheets (i.e., $k_{f\mathrm{M}}$). A close examination of the energy landscapes of the non-rigid unit cell shows that the multi-stability is sequentially achieved as the ratio of $k_{f\mathrm{C}}/k_{f\mathrm{M}}$ increases.

Overall, this study introduces dimensionless rigidity parameters (i.e., α and β) to the nonlinear bar-hinge model. With that, one can quantitatively study the mechanics of non-rigid origami by strategically manipulating its facet compliance. To this end, we discuss the multi-stability of an origami unit cell by intentionally relax the rigid-folding conditions. By showing the benefits of exploiting facet compliance, this study could foster multi-functional structures and material systems that traditional rigid origami cannot create.

ACKNOWLEDGMENT

The authors acknowledge the partial support from the National Science Foundation (Award # CMMI-1751449 CAREER) and Clemson University (via startup funding and the CECAS Dean's Faculty Fellow Award).

REFERENCES

[1] Nadkarni, N., Arrieta, A. F., Chong, C., Kochmann, D. M., and Daraio, C., 2016. "Unidirectional Transition Waves in Bistable Lattices". *Physical Review Letters,* ***116***(24), jun, p. 244501.

[2] Raney, J. R., Nadkarni, N., Daraio, C., Kochmann, D. M., Lewis, J. A., and Bertoldi, K., 2016. "Stable propagation of mechanical signals in soft media using stored elastic energy". *Proceedings of the National Academy of Sciences,* ***113***(35), aug, pp. 9722–9727.

[3] Daynes, S., and Weaver, P. M., 2013. "Review of shape-morphing automobile structures: concepts and outlook". *Proceedings of the Institution of Mechanical Engineers, Part D: Journal of Automobile Engineering,* ***227***(11), nov, pp. 1603–1622.

[4] Florijn, B., Coulais, C., and van Hecke, M., 2014. "Programmable Mechanical Metamaterials". *Physical Review Letters,* ***113***(17), oct, p. 175503.

[5] Kidambi, N., Harne, R. L., and Wang, K. W., 2016. "Adaptation of Energy Dissipation in a Mechanical Metastable Module Excited Near Resonance". *Journal of Vibration and Acoustics,* ***138***(1), feb, pp. 1–9.

[6] Harne, R., and Wang, K., 2014. "A bifurcation-based coupled linear-bistable system for microscale mass sensing". *Journal of Sound and Vibration,* ***333***(8), apr, pp. 2241–2252.

[7] Kim, S.-W., Koh, J.-S., Lee, J.-G., Ryu, J., Cho, M., and Cho, K.-J., 2014. "Flytrap-inspired robot using structurally integrated actuation based on bistability and a developable surface". *Bioinspiration & Biomimetics,* ***9***(3), mar, p. 036004.

[8] Sun, J., Guan, Q., Liu, Y., and Leng, J., 2016. "Morphing aircraft based on smart materials and structures: A state-of-the-art review". *Journal of Intelligent Material Systems and Structures,* ***27***(17), oct, pp. 2289–2312.

[9] Harne, R. L., and Wang, K. W., 2013. "A review of the recent research on vibration energy harvesting via bistable systems". *Smart Materials and Structures,* ***22***(2), feb, p. 023001.

[10] Li, S., Fang, H., Sadeghi, S., Bhovad, P., and Wang, K.-W., 2019. "Architected Origami Materials: How Folding Creates Sophisticated Mechanical Properties". *Advanced Materials,* ***31***(5), feb, p. 1805282.

[11] Waitukaitis, S., Menaut, R., Chen, B. G.-g., and van Hecke, M., 2015. "Origami Multistability: From Single Vertices to Metasheets". *Physical Review Letters,* ***114***(5), feb, p. 055503.

[12] Schenk, M., and Guest, S. D., 2013. "Geometry of Miura-folded metamaterials". *Proceedings of the National Academy of Sciences,* ***110***(9), feb, pp. 3276–3281.

[13] Li, S., Fang, H., and Wang, K. W., 2016. "Recoverable and Programmable Collapse from Folding Pressurized Origami Cellular Solids". *Physical Review Letters,* ***117***(11), sep, p. 114301.

[14] Fang, H., Wang, K., and Li, S., 2017. "Asymmetric energy barrier and mechanical diode effect from folding multi-stable stacked-origami". *Extreme Mechanics Letters,* ***17***, nov, pp. 7–15.

[15] Yasuda, H., Chen, Z., and Yang, J., 2016. "Multitransformable Leaf-Out Origami With Bistable Behavior". *Journal of Mechanisms and Robotics,* ***8***(3), jun, p. 031013.

[16] Sadeghi, S., and Li, S., 2020. "Dynamic Folding of Origami By Exploiting Asymmetric Multi-Stability". *arXiv*, jun, pp. 1–24.

[17] Kaufmann, J., and Li, S., 2020. "Harnessing The Multi-Stability Of Kresling Origami For Reconfigurable Articulation In Soft Robotic Arms". *arXiv*, aug.

[18] Ma, J., Zang, S., Feng, H., Chen, Y., and You, Z., 2021. "Theoretical characterization of a non-rigid-foldable square-twist origami for property programmability". *International Journal of Mechanical Sciences,* ***189***(July 2020), jan, p. 105981.

[19] Kamrava, S., Ghosh, R., Wang, Z., and Vaziri, A., 2019. "Origami-Inspired Cellular Metamaterial With Anisotropic Multi-Stability". *Advanced Engineering Materials,* ***21***(2), feb, p. 1800895.

[20] Liu, K., and Paulino, G. H., 2018. "Highly efficient nonlinear structural analysis of origami assemblages using the MERLIN2 software". *The proceedings from the seventh meeting of Origami, Science, Mathematics and Education.*

[21] Baharisangari, N., and Li, S., 2019. "Exploiting the Asymmetric Energy Barrier in Multi-Stable Origami to Enable Mechanical Diode Behavior in Compression". In Volume 5B: 43rd Mechanisms and Robotics Conference, Vol. 5B-2019, American Society of Mechanical Engineers, pp. 1–8.

[22] Liu, K., and Paulino, G. H., 2017. "Nonlinear mechanics of non-rigid origami: an efficient computational approach". *Proceedings of the Royal Society A: Mathematical, Physical and Engineering Sciences,* ***473***(2206), oct,

p. 20170348.

[23] Li, S., and Wang, K. W., 2015. "Fluidic origami with embedded pressure dependent multi-stability: a plant inspired innovation". *Journal of The Royal Society Interface,* ***12***(111), oct, p. 20150639.

[24] Liu, K., Tachi, T., and Paulino, G. H., 2019. "Invariant and smooth limit of discrete geometry folded from bistable origami leading to multistable metasurfaces". *Nature Communications,* ***10***(1), dec, p. 4238.

[25] Gillman, A., Fuchi, K., and Buskohl, P., 2018. "Truss-based nonlinear mechanical analysis for origami structures exhibiting bifurcation and limit point instabilities". *International Journal of Solids and Structures,* ***147***, aug, pp. 80–93.

[26] Li, S., and Wang, K. W., 2015. "Fluidic origami: a plant-inspired adaptive structure with shape morphing and stiffness tuning". *Smart Materials and Structures,* ***24***(10), oct, p. 105031.

[27] Filipov, E., Liu, K., Tachi, T., Schenk, M., and Paulino, G., 2017. "Bar and hinge models for scalable analysis of origami". *International Journal of Solids and Structures,* ***124***, oct, pp. 26–45.